Key issues in the microchemical systems-based methanol fuel processor: Energy density, thermal integration, and heat loss mechanisms

Keyur Shah, R.S. Besser *

*New Jersey Center for Microchemical Systems, Department of Chemical, Biomedical and Material Engineering,
Stevens Institute of Technology, Castle Point on Hudson, Hoboken, NJ 07030, United States*

Abstract

Microreactor technology is a promising approach in harnessing the high energy density of hydrocarbons and is being used to produce hydrogen-rich gases by reforming of methanol and other liquid hydrocarbons. However, on-demand H_2 generation for miniature proton exchange membrane fuel cell (PEMFC) systems has been a bottleneck problem, which has limited the development and demonstration of the PEMFC for high-performance portable power. A number of crucial challenges exist for the realization of practical portable fuel processors. Among these, the management of heat in a compact format is perhaps the most crucial challenge for portable fuel processors. In this study, a silicon microreactor-based catalytic methanol steam reforming reactor was designed, fabricated, and demonstrated in the context of complete thermal integration to understand this critical issue and develop a knowledge base required to rationally design and integrate the microchemical components of a fuel processor. Detailed thermal and reaction experiments were carried out to demonstrate the potential of microreactor-based on-demand H_2 generation. Based on thermal characterization experiments, the heat loss mechanisms and effective convective heat coefficients from the planar microreactor structure were determined and suggestions were made for scale up and implementation of packaging schemes to reduce different modes of heat losses.

© 2007 Elsevier B.V. All rights reserved.

Keywords: Portable power; Microreactor; PEMFC; Fuel processing; Methanol steam reformer; Thermal management

1. Introduction

As fuel cell (FC) gain attention as potential energy solution of the future, one of the most promising fields of application is portable power, as a prominent alternative to batteries [1]. Batteries are a multi-billion dollar market and the technology has made significant strides in the last couple of decades to meet growing power demand of advanced portable computing, handheld personal devices, and other microelectronics systems. The rechargeable battery technology has progressed from nickel cadmium (NiCD) to nickel meta hydride (NiMH) to lithium ion (Li-Ion). Until recently, the gradual improvement of Li-based batteries was enough to power mobile computing devices. Unfortunately, the energy density available from current battery technology is inadequate to match the power demands of emerging portable devices [2]. This need has encouraged researchers to continue to vigorously explore FCs as miniature power sources.

High energy density is required for advanced portable applications for consumer use (e.g., laptop computers, PDAs, cellular phones, medical and telecommunication devices), and for military and intelligence use (e.g., remote sensors (<20 W), systems for the soldier (<500 W), silent power generation and battery recharging (200 W–2 kW), and mobile power generation and auxiliary power units (>2 kW)) [3], with the goal of allowing these devices to operate for longer times with less recharging. Miniatures FCs offer promise for the conversion of chemical energy into electrical energy in a highly efficient way achieving the goals of power dense, light weight, and compact power sources.

The proton exchange membrane fuel cell (PEMFC) is particularly attractive and promising for portable applications because of its ability to provide high power density and nearly instant power. Moreover, its simplicity in design and operation allow-

* Corresponding author. Tel.: +1 201 216 5257; fax: +1 201 216 8306.
  E-mail address: rbesser@stevens.edu (R.S. Besser).

Nomenclature

A	surface area (m^2)
A_w	cross-sectional area of the wire (m^2)
c_MeOH	methanol concentration in feed (mol cm^{-3})
d_h	hydraulic diameter (m)
D_AB	diffusivity of methanol in gas mixture $(\text{m}^2\,\text{s}^{-1})$
E	Emissive power (W m^{-2})
$E_{\text{b}\lambda}$	spectral blackbody emissive power $(\text{W m}^{-2}\,\mu\text{m}^{-1})$
h	heat transfer coefficient $(\text{W m}^{-2}\,\text{K}^{-1})$
I	current (A)
I_λ	radiative intensity $(\text{W m}^{-2}\,\text{s}^{-1})$
k_g	mass transfer coefficient (m s^{-1})
k_λ^Py	spectral absorption coefficient of Pyrex$^{\text{TM}}$ (m^{-1})
k_λ^Si	spectral absorption coefficient of silicon (m^{-1})
l	length of the wire (m)
N_Nu	Nusselt number
N_Ra	Rayleigh number
P'	perimeter of the wire (m)
$Q_\text{conv.}$	heat loss by convection
Q_in	heat input (W)
Q_loss	total heat loss (W)
$Q_\text{rad.}$	heat loss by radiation
Q_wires	heat loss from the attached wires
r_MeOH	methanol reaction rate $(\text{mol cm}^{-3}\,\text{s}^{-1})$
Sh	Sherwood number
T_s	surface temperature (K)
T_∞	ambient temperature (K)
V	voltage (V)

Greek letter

α	constant used in equation (5)

ing fabrication of a compact and lightweight cell, mild operating conditions (temperature less then $100\,^\circ\text{C}$, pressure in the range of a few atmospheres), and relatively low loading of precious metal catalysts are additional strong advantages [1,4].

The success of PEMFC technology for portable power depends heavily on the development of efficient ways of delivering the appropriate fuel to the cell. The PEMFC operating on hydrogen as the fuel holds the most promise, offering the best possible efficiency and power density [5,6]. However, while hydrogen offers high energy density on a per weight basis, it has a poor energy density per volume. Gaseous hydrogen is therefore difficult and inefficient to store and several high energy density storage methods have been investigated such as highly pressurized cylinders, metal hydrides, chemical hydrides, and even carbon nanotubes [7,8]. Since on-board storage of hydrogen is unsafe and energy inefficient, two main alternatives are commonly envisioned and employed for portability.

One approach, the direct FC employs fuels like methanol, ethanol, formic acid, etc., directly in the cell to generate electricity. The direct FC has the advantage of a smaller total system and weight, as it does not 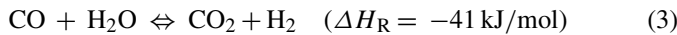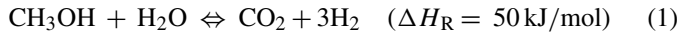need an in-situ fuel processing (FP) unit to extract hydrogen. Among all direct FCs investigated at the portable scale, more research and development efforts are focused on the development of direct methanol fuel cell (DMFC). Several groups are pursuing low power DMFCs for portable power applications [9]. Although the DMFC offers promising possibilities as a miniature power source, the technology has to overcome a number of challenges to be competitive with battery technology in terms of efficiency, power density, and cost. Methanol crossover and the relatively slow reaction rate of methanol oxidation to hydrogen ions and carbon dioxide at the anode are persisting challenges that currently limit the DMFC to less stringent applications. In addition to DMFC, the direct ethanol fuel cell (DEFC) and direct formic acid fuel cell (DFAFC) are also being developed. Ethanol is considered an attractive fuel mainly because of its higher theoretical energy density than methanol, non-toxicity, availability, and renewability [10,11]. However, the available power density from DEFC is currently about half that of DMFC resulting from relatively slower electrooxidation reaction kinetics at the anode. Recently, the DFAFC has been demonstrated as an attractive alternative [12]. The theoretical energy density of formic acid is less than one-third of methanol. However, formic acid has other advantages like faster anode kinetics and smaller crossover through Nafion membranes. Unlike DMFC where methanol crossover limits the use of higher methanol concentration solutions, it is possible to run the DFAFC with high concentrations of formic acid. However, it was recently observed that the performance of the cell dropped as the formic acid concentration was increased beyond $10\,\text{M}$ because of decreases in anode catalytic activity and an increase of the fuel crossover [13].

The other, higher performance alternative is to generate pure hydrogen on site and on demand by processing easily stored, high energy density liquid fuels [14]. FP adds complexity, weight, volume, and cost compared to the DMFC or a system running directly on hydrogen, however the effective energy storage density is significantly higher.

A wide variety of energy dense hydrocarbons such as natural gas, methanol, gasoline, and diesel can be reformed into hydrogen-rich streams for FCs. Different processes are available for hydrogen extraction and subsequent purification, therefore, the type of hydrocarbon and method used to produce the hydrogen play a major role in the design of a FP system. Processing of liquid hydrocarbons to hydrogen involves a series of steps including fuel vaporization, reforming (three main processes available are partial oxidation, steam reforming (SR), and autothermal reforming), water gas shift (WGS), and CO clean up (preferential oxidation (PrOx), hydrogen separation by permeation through a hydrogen-selective membrane, or pressure swing adsorption) before feeding hydrogen rich gases to the FC.

Methanol is the fuel of choice for mobile portable power application as it is sulfur free and can be reformed at relatively low temperatures (250–$300\,^\circ\text{C}$), simplifying the micro FP design. Moreover, it offers other advantages like high hydrogen–carbon ratio, high energy density, and ready availability.

The following chemical reactions take place during the SR process.

$$CH_3OH + H_2O \Leftrightarrow CO_2 + 3H_2 \quad (\Delta H_R = 50\,kJ/mol) \qquad (1)$$

$$CH_3OH \Leftrightarrow CO + 2H_2 \quad (\Delta H_R = 90\,kJ/mol) \qquad (2)$$

$$CO + H_2O \Leftrightarrow CO_2 + H_2 \quad (\Delta H_R = -41\,kJ/mol) \qquad (3)$$

Eq. (1) is the main reforming reaction, Eq. (2) is the methanol decomposition reaction, while the third equation represents the water–gas shift reaction. The reforming reaction is endothermic in nature and thus requires external energy. Also energy is required to vaporize and superheat the methanol–water mixture to the desired SR reaction temperature. These requirements can be reasonably met by combusting excess hydrogen from the anode exhaust of the FC. The catalytic SR of methanol on a CuO/ZnO based catalyst is a highly efficient process, producing a reformate with high hydrogen concentration (65–70%) while maintaining high CO_2 selectivity compared to other available reforming processes. A CO concentration of 1–2% is attained while operating at temperatures ranging from 220 to 260 °C as a consequence of reaction thermodynamics [15,16]. Therefore a methanol-based FP system must include a CO clean up step, as this relatively low level of CO is still enough to poison the PEMFC catalyst. However, the low CO concentration eliminates the need for WGS, requiring only a PrOx step to reduce CO below 10 ppm.

2. Microscale FP: issues and challenges

A block diagram for an overall system was developed and is shown in Fig. 1. The system burns the unconverted hydrogen from the FC anode in the combustor to supply the heat required for vaporizing the methanol-water feed and to carry out the endothermic reforming reaction. The total system includes key microreactor components (combustor, vaporizer, SR, and PrOx reactor), FC stack, a diluted methanol storage tank (water recycling is not employed for simplicity), a rechargeable battery

for start up and rapid load following, insulation, and peripheral components. In addition, a separate storage of pure methanol is required as an additional fuel in the combustor if the unconverted anode hydrogen does not meet the energy requirement for vaporizer and SR.

Considerable efforts have been made to develop an integrated FP/FC system, however, several issues and challenges persist. Based on the literature and our own research, many of these key issues are identified and discussed in our previous paper [17]. Among them, miniaturization of system components and thermal management are perhaps the most crucial. In order to understand the relationships and tradeoffs of these issues, a study encompassing energy density, component sizing, and thermal integration of key FP components was performed.

2.1. Analysis of energy density with methanol-based FP/FC system

Energy density is the ratio of energy available from a power source to its volume (usually quoted in $Wh\,l^{-1}$) or weight ($Wh\,kg^{-1}$), while for a fuel it is the amount of energy that can be contained in a specific quantity of the fuel itself.

Pure methanol has an energy density of $4380\,Wh\,l^{-1}$ ($5600\,Wh\,kg^{-1}$), which is about 15 times the projected energy density of a Li-ion secondary battery ($300\,Wh\,l^{-1}$), meaning that the FP/FC unit has superior energy density even with an overall conversion efficiency as low as 7%. In the case where no water recycling is employed to minimize system complexity, water has to be carried with methanol for the reforming. With a stoichiometric steam to carbon ratio of 1:1, this reduces the net energy density to $3000\,Wh\,l^{-1}$ ($4550\,Wh\,kg^{-1}$).

The energy density comparison between methanol-based FC technology with batteries illustrates the potential of this technology for the consumer portable market. If an advanced cell phone device consuming 1 W is powered by a 50 ml methanol
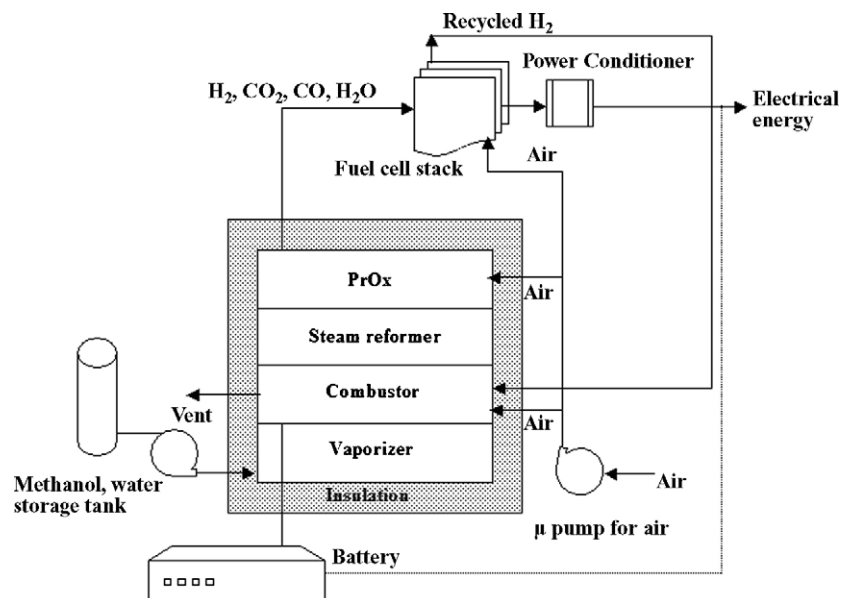

Fig. 1. Block diagram for converting methanol to electricity using an integrated FP/FC system.

Table 1
Energy density at various mission durations

Mission duration	DARPA goal (Wh kg^{-1})	Weight (kg) of FP/FC[a] (energy density, Wh kg^{-1})	Weight of BA 5590[b] (kg)	Weight ratio (FP/FC)/BA 5590
3 h, 60 Wh	1000	0.55 (110)	0.35	1.57
3 days, 1440 Wh	2000	1.75 (820)	8.32	0.21
10 days, 4800 Wh	3000	4.70 (1020)	27.75	0.17

Based on DARPA expectations and estimated from methanol-based FP/FC integrated system.

[a] Weight of FP/FC excluding (methanol + water) storage: 500 g.

[b] BA 5590, a lithium-ion battery (energy density of 170 Wh kg^{-1}) is a widely used battery for military applications.

cartridge, and considering only 10% overall efficiency, a continuous transmission time of 22 h without recharge is possible. This represents a significant gain relative to current capabilities.

A number of military applications have been identified which represent a significant market for miniature power. The Department of Defense (DoD) seeks lighter and more compact electrical power sources for individual soldier, robotic, and other combat missions. The higher energy density will allow soldiers to carry less weight and to extend mission duration.

In 2002, DARPA set the energy density goals for three mission scenarios at an average power level of 20 W [18], which are listed in Table 1. The expected specific energy includes the total system and fuel.

If we assume an optimistic conversion efficiency (which includes FP conversion efficiency and FC efficiency) of 25%, available energy density would be 1140 Wh kg^{-1}. It is possible to determine whether methanol-based systems can meet energy density expectations set by DARPA for different missions assuming the conditions listed in the caption to Table 1. This comparison is shown in Table 1. We see clearly that DARPA has set aggressive energy density expectations for these missions, which can only be achieved with diesel or other high energy density hydrocarbons; or perhaps with alternative technologies.

Table 1 also shows the comparison between the weights of the BA 5590 battery versus a methanol FP/PEMFC system. Net energy density increases favorably for extended missions since only fuel is added to increase the duration. As shown in Table 1 missions of 10-day duration result in a net energy density of 1020 Wh kg^{-1}, which is a six times improvement over the BA5590 (170 Wh kg^{-1}).

2.2. Miniaturization: microchemical systems for microscale FP

Microchemical systems have the potential for highly compact power sources through integration of a FC with all the unit operation components of a FP along with microstructured sensors, actuators and other "balance of plant" (BOP) devices. [19]. Their microscale dimensions result in high heat and mass transfer rates [20], making them efficient in applications where it is necessary to thermally couple endothermic and exothermic processes. The excellent transport and low thermal mass ensure short times to reach working temperature at start-up.

2.3. Miniaturization: component sizing and compatible catalyst technology

The initial objective of our group's research efforts was to perform a model-based design and integration study of microchannel reactor components of a fuel-processing unit for converting methanol to hydrogen with <10 ppm CO for a 20W_e PEMFC. The ASPEN PLUS^{TM} process simulator was used to simulate the overall FP/PEMFC system. The ASPEN analysis provided major operating parameters such as temperatures, pressures, and flow rates needed to carry out a preliminary design for key FP microreactor components as a first order estimate of the size requirements for the 20W_e micro FP [21].

The SR, combustor, and PrOx microreactors were designed based on a thin-film catalyst approach [22], which consists of a ~10 μm layer of catalyst deposited on microchannel walls. For the preliminary design of the SR and combustor, a kinetic model based on power-law rate expressions from the literature were used [23,24]. The PrOx microreactor design is based on our own kinetic experimental data as our group has successfully demonstrated a 0.25W_e single channel silicon microreactor with Pt/Al$_2$O$_3$ thin-film wall catalyst for PrOx of CO in hydrogen rich reformate [25]. This modeling approach estimated the catalyst loading for each of the microreactor components, which helped determine other microreactor design details such as size and number of microchannels required, overall reactor layer size and geometry, and the number of layers to be stacked, etc. The process parameters and the design results for each component are listed in Table 2.

Miniaturization of each component by reducing weight and volume and high-energy efficiency were the main objective of this work. Due to different demands placed on the different reaction steps, there are different requirements for the catalysts for each of the components. The sizing estimates show that the thin film catalyst approach can be used for PrOx and combustor microreactors but it is not favorable for the SR microreactor at this scale, based on the achievable loading. Note that the combustor required the least amount of catalyst loading, such that a single Pt wire would be sufficient.

The results obtained from the above 1D sizing-analysis showed that the SR is the largest component and it drives the overall size of the micro FP. The SR reaction is relatively slow and hence needs larger amounts of catalyst at this temperature range to achieve high conversion. It is not possible to load a sufficient catalyst amount to further miniaturize the SR if the thin

Table 2
Preliminary sizing estimates: process parameters and design results

Component	Process parameters and design results
SR	W_e, 60% FC efficiency, 75% H_2 utilization MeOH conversion 100% $F_{MeOH} = 6.233e{-}5 \, mol \, s^{-1}$ $F_{H_2O} = 8.10e{-}5 \, mol \, s^{-1}$ $H_2O{:}MeOH = 1.3{:}1$ 260 °C 1 atm Microchannel: 50 µm × 400 µm Parallel microchannels: 1000 Channel to channel spacing: 50 µm Reaction zone width: 10 cm Catalyst film: Cu/ZnO/Al$_2$O$_3$, 5 µm thickness (0.0478 g cm^{-1}) Reactor layers: 24 Total catalyst loading: 2.87 g
PrOx	160 °C Catalyst film: Pt/Al$_2$O$_3$, 5 µm thickness (0.0478 g cm^{-1}) CO in reformate: 2.2% Reactor layers: 9 Total reactor loading: 1.1 g
Combustor	Off gas recycle to combustor: 2.5e$-$4 mol s^{-1} Gas composition: H$_2$: 33.8%, CO$_2$: 38.8%, H$_2$O: 11.8%, O$_2$: 0.6%, and N$_2$: 15.1% Total catalyst loading: 1.2 mg

film approach is used. Thus a different approach to incorporate catalyst into the small reaction zone of microreactor at higher loading is needed. Packing the reformer with catalyst powder and use of a foam-based cellular catalyst [26], offering significantly higher loading than thin-films are other options that were also considered.

2.4. Thermal management in microscale FP

Thermal management in miniature systems is perhaps the most crucial challenge for microscale FPs. Thermal coupling is needed to allow transfer of energy from the heat producing combustor to the endothermic SR. Coupling endothermic and exothermic components and minimizing losses promotes a high thermal efficiency. However, such coupling must be accomplished in a manner that permits the maintenance of specific temperatures in the various components as shown in Fig. 2 and maintains the surface of the package near room temperature. Microreactors generally offer high heat transfer rates mainly because of high surface-to-volume ratio, short conduction paths, and high thermal conductivity of materials used. This characteristic results in efficient heat transfer between the different processing steps but at the same time results in higher heat losses to the ambient. Therefore, thermal management offers a dual challenge of opposing the heat losses from the system that arise from high surface-to-volume ratio in conjunction with maintaining temperature gradients within the system to allow desired conditions in the unit reaction steps.

Different materials have been used for the construction of microscale FP components, including metal [27–29], silicon
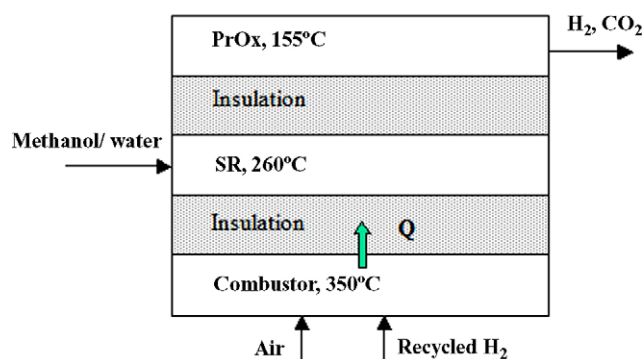

Fig. 2. Integration of fuel processing components.

[30–33], ceramic [34], and glass [35]. However, all the materials approaches are confronted with the thermal management issues described above. Because microfabrication processes leverage two-dimensional replication technologies like photolithography, a flat, sheet-like architecture is the norm for microfabricated components of FPs. This kind of low aspect ratio, planar architecture offers an excellent inter-component heat transfer, but is poor for heat retention and results in significant losses to the ambient.

3. Thermal management: demonstration of an integrated SR

To address the crucial issue of heat management, we present the development of a silicon microreactor based methanol SR with emphasize on thermal integration of the overall system. As shown in Fig. 3, a silicon micro SR was designed and integrated with microfabricated insulation as dictated by an overall system design. An integrated design was made where thin metal film heaters and temperature sensors were directly embedded into the unit. External heat was introduced to simulate integration with a combustor. Detailed thermal data (heat input required, heat losses, temperature profiles) and reaction data (conversion and selectivity) were acquired.

Because of its various advantages, silicon microfabrication technology was employed in this work to achieve miniaturization. However, our intent was to perform thermal and reaction experiments whose outcome depends most critically on microscale geometry and less so on the materials of construction. In this way the results obtained may be generalizable to any of the materials technologies. Silicon is a reasonable material choice as it is lighter than stainless steel and possesses high mechanical
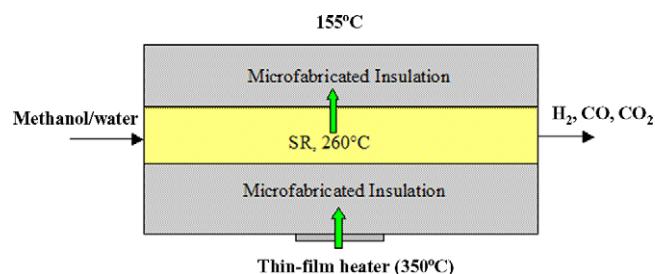

Fig. 3. Demonstration of thermally integrated SR.

strength, chemical inertness, thermal stability, and large thermal conductivity. With the established silicon microfabrication technology, it is possible to create novel microchannel and reactor configurations in the sub-millimeter range. An important advantage of silicon microfabrication is its compatibility with thin film technology. This facilitates eventual on-chip integration of functional elements like sensors and actuators allowing compact process control subsystems.

3.1. Design of a micro methanol SR

A silicon microreactor with a reaction zone of $1\,\text{cm} \times 1\,\text{cm} \times 400\,\mu\text{m}$ ($0.04\,\text{cm}^3$) was designed. The design incorporates a packed bed of commercial copper-based powder catalyst. The packing of the reaction bed resulted in a catalyst loading of 50 mg calculated using the bulk density of the catalyst. A kinetic model was formulated using an Arrhenius type power-law rate expression for methanol reforming over a $Cu/ZnO/Al_2O_3$ catalyst [23], assuming no mass transfer resistance. Using this model, with the knowledge of reaction temperature and catalyst load-

ing, methanol and water flows (S/C molar ratio of 1.3:1) were determined to achieve essentially 100% conversion of methanol. Using a methanol flow rate of $1.32\text{e}{-}4\,\text{mol}\,\text{min}^{-1}$ at $260\,^\circ\text{C}$, the reaction produces $3.84\text{e}{-}4\,\text{mol}\,\text{min}^{-1}$ (9 sccm) of hydrogen, which was sufficient to produce 0.65 W from a FC assuming 60% efficiency and 75% hydrogen utilization in the FC.

Fig. 4(a) shows the design of the SR microreactor. The reactor consisted of an inlet to introduce the mixture of vaporized methanol and steam, an outlet to remove reformate, a packed bed reaction zone, flow manifold structure, and filter structures at the outlet to trap catalyst particles.

Pressure drop for the reaction zone packed with catalyst was estimated from the Ergun equation [36]. For catalyst particles of $75\,\mu\text{m}$, the reactor of 1-cm bed length resulted in a nearly insignificant pressure drop of 190 Pa. This low pressure drop is consistent with the low superficial velocity resulting from the flow rates of gaseous reactants through the 1-cm wide $\times$ $400\,\mu\text{m}$ high cross-section. Low pressure drop across the bed can lead to maldistribution of flow and the resulting non-uniform catalyst utilization and residence time. In order to avoid this situation,
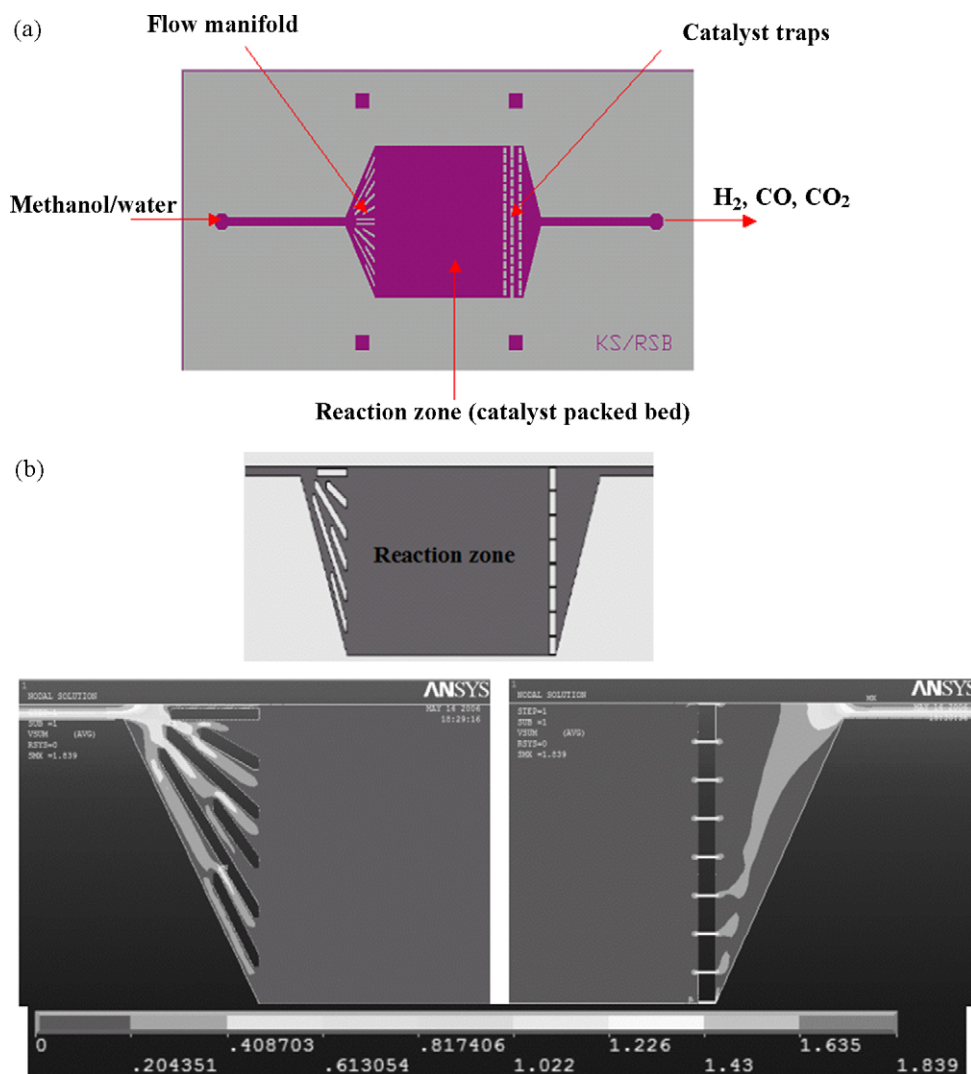

Fig. 4. (a) Design of the SR microreactor. (b) 2D axisymmetric flow model used in CFD simulation and velocity distribution in microreactor.

an inlet manifold structure was designed to obtain uniform flow distribution across the reaction zone width. The manifold channels were designed to ensure that catalyst particles easily flow into the reaction zone during loading. The FLOTRAN CFD simulation package in ANSYS Multiphysics software was used to determine the velocity profile across the reaction zone for a given boundary condition of flow velocity at the inlet with an outlet boundary condition of atmospheric pressure. Fig. 4(b) shows the 2D axisymmetric flow model and the velocity profile along the packed bed.

3.2. Internal heat management: thermal coupling and design of insulation

In order to maintain desired temperature gradients between FP components, insulators are required to bridge the temperature differences. The goal was to design insulation such that it adds little to the weight and volume of the total system and can be integrated with microfabrication. The high surface-to-volume ratio of microreactors, high thermal conductivity of silicon, and sub-millimeter conduction paths make it difficult to obtain the desired thermal isolation between components. It is therefore, necessary to employ special structures like thin suspended membranes, vacuum gaps, or insulating materials with ultra low thermal conductivity to bridge these temperature differences and to minimize conductive and convective heat losses to the surroundings.

The best commercial insulators have thermal conductivities in the range of 0.02 W mK^{-1} and are difficult to integrate into a microfabricated unit. However, vacuum packaging of microreactors can provide an effective means of insulation. From the kinetic theory of gases, it is known that the thermal conductivity of a gas is approximately independent of pressure for atmosphere and above [37], and decreases with sub-atmospheric pressures, as the mean free path becomes less than the enclosure dimensions [38]. Fig. 5(a) shows a plot of k_p/k_0 (k_p being thermal conductivity of air at sub-atmospheric pressure [39] and k_0 being thermal conductivity of air at atmospheric pressure) versus sub-atmospheric pressures for a cavity depth of 500 μm. A microfabricated cavity surrounding the reactor filled with low-pressure gas offers low thermal conductivity down to approximately 0.001 W mK^{-1}. Silicon microfabrication enables a straightforward approach to this structure, as the cavity etched in silicon can be sealed to trap the desired level of vacuum and the desired residual gas species. Fig. 5(b) shows the concept for integrating vacuum insulation.

3D thermal simulation using ANSYS® simulation software was carried out to design microfabricated vacuum insulation such that it can maintain the required temperature gradients. The simulation also determined placement of the combustor and PrOx zones in reference to the reformer reaction zone, pressure in the cavity and the depth of cavity required. As noted earlier, the reforming microreactor was designed to produce $3.84e{-}4 \text{ mol min}^{-1}$ of hydrogen. Considering 75% hydrogen
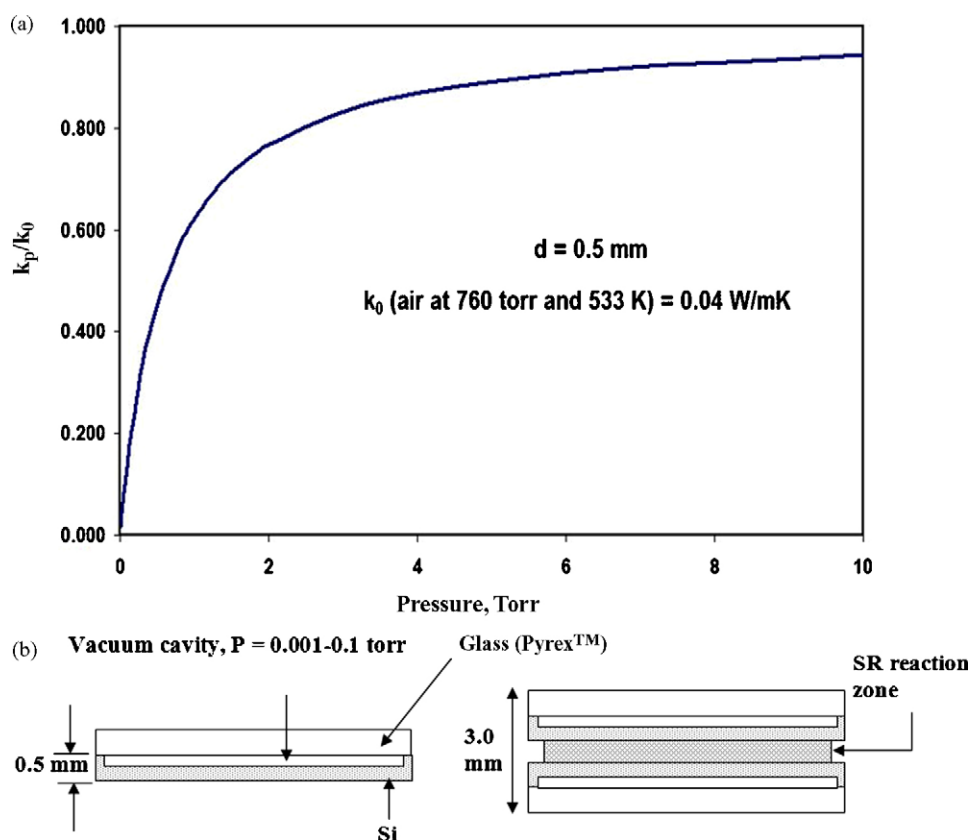

Fig. 5. (a) Thermal conductivity of air at sub-atmospheric pressures for a cavity depth of 500 μm. (b) Vacuum insulation chip with a single microfabricated cavity in Si, and reformer reaction zone sandwiched between insulation chips.
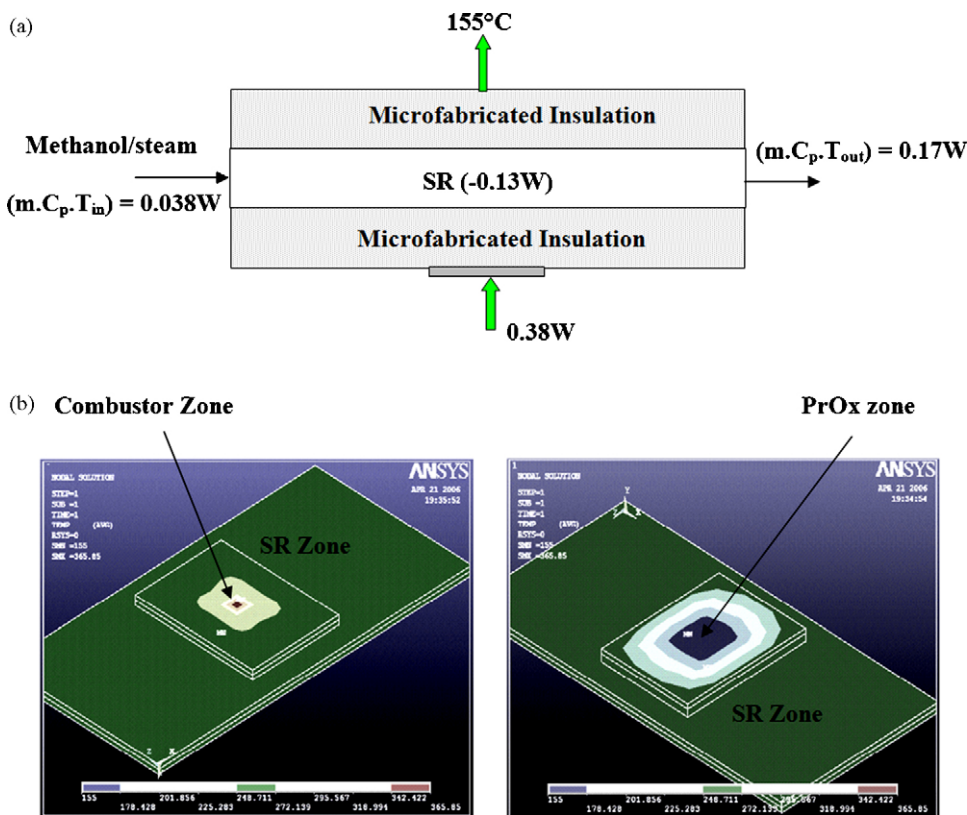
Fig. 6. (a) The concept of 3D thermal model used to design microfabricated vacuum insulation. (b) 3D thermal simulation results showing the temperature distribution in different compartments.

utilization in the FC, the remaining $9.6\mathrm{e}{-}5$ mol min^{-1} of hydrogen in the anode effluent when burned, gives 0.38 W based on the lower heating value of hydrogen. The temperature boundary conditions, endothermic heat of reforming, and reactant and product sensible heats used in the 3D model are shown in Fig. 6(a) while Fig. 6(b) shows the result. The simulation yielded the temperature distributions in each of the compartments. Thermal conductivity of air in the cavity was varied until the required component temperatures were achieved. For generality, the model did not consider heat losses.

3.3. Design and fabrication of an integrated SR

The design of the integrated SR is shown in Fig. 7(a). The stack of six chips consisted of insulation chips surrounding the reforming microreactor. The silicon reactor was covered on the top with a Pyrex$^{\mathrm{TM}}$ sheet of the same lateral dimensions. Thin film resistance temperature detector (RTD) sensors were patterned at different positions on the backside of the silicon microreactor. Three sensors were placed at different positions to measure the reaction zone temperature distribution and one each was placed at the inlet and outlet section as shown in the superimposed image (Fig. 7(b)) of the front and backside CAD masks of the microreactor. The sensors have meandering resistors with a four-wire design to minimize lead resistance effects. The insulation consisted of an assembly of silicon and glass chips. The silicon chip had a cavity in the center and was bonded with Pyrex$^{\mathrm{TM}}$ heater and temperature sensor substrate as shown

in Fig. 7(c). The relative sizes of the combustor and PrOx units were determined from the initial size estimation discussed in Section 2.3. The insulation requirements, described next, were determined based on thermal and structural considerations.

The insulation requirement between the combustor and the reformer is not demanding, as the reformer needs endothermic heat of reaction. An appropriate thermal conductivity and insulating thickness is obtained in this case by a 50-μm deep cavity containing air at atmospheric pressure. The lateral dimensions of the silicon and glass are thus 1.1 cm × 1.4 cm while the cavity is slightly smaller at 1.0 cm × 1.3 cm. The combustor is 2.8 mm × 2.8 mm and is centered over an insulation chip keeping a lateral distance of 7.2 mm × 10.2 mm from conducting vertical paths. An integrated on-chip thin-film Pt heater meandering along this area is used to simulate the combustor. Three thin-film temperature sensors are also patterned on the glass chip. One sensor was located right in the center of the combustor zone, while two others were placed on either side at a distance of 600 μm from the center.

On the opposite side of the assembly, more stringent thermal isolation is required between the reformer and the PrOx. For this reason, the insulation between the reformer and the PrOx had a 200-μm deep cavity and was sealed with vacuum of less than 5.10^{-3} Torr. The silicon insulation chip of lateral dimensions 1.2 cm × 1.5 cm had a cavity of 1.1 cm × 1.4 cm. The effective insulation in this case requires higher vacuum, a deeper cavity, and smaller conductive distance between the cavity and the insulation chip. Since silicon has a high thermal conductivity
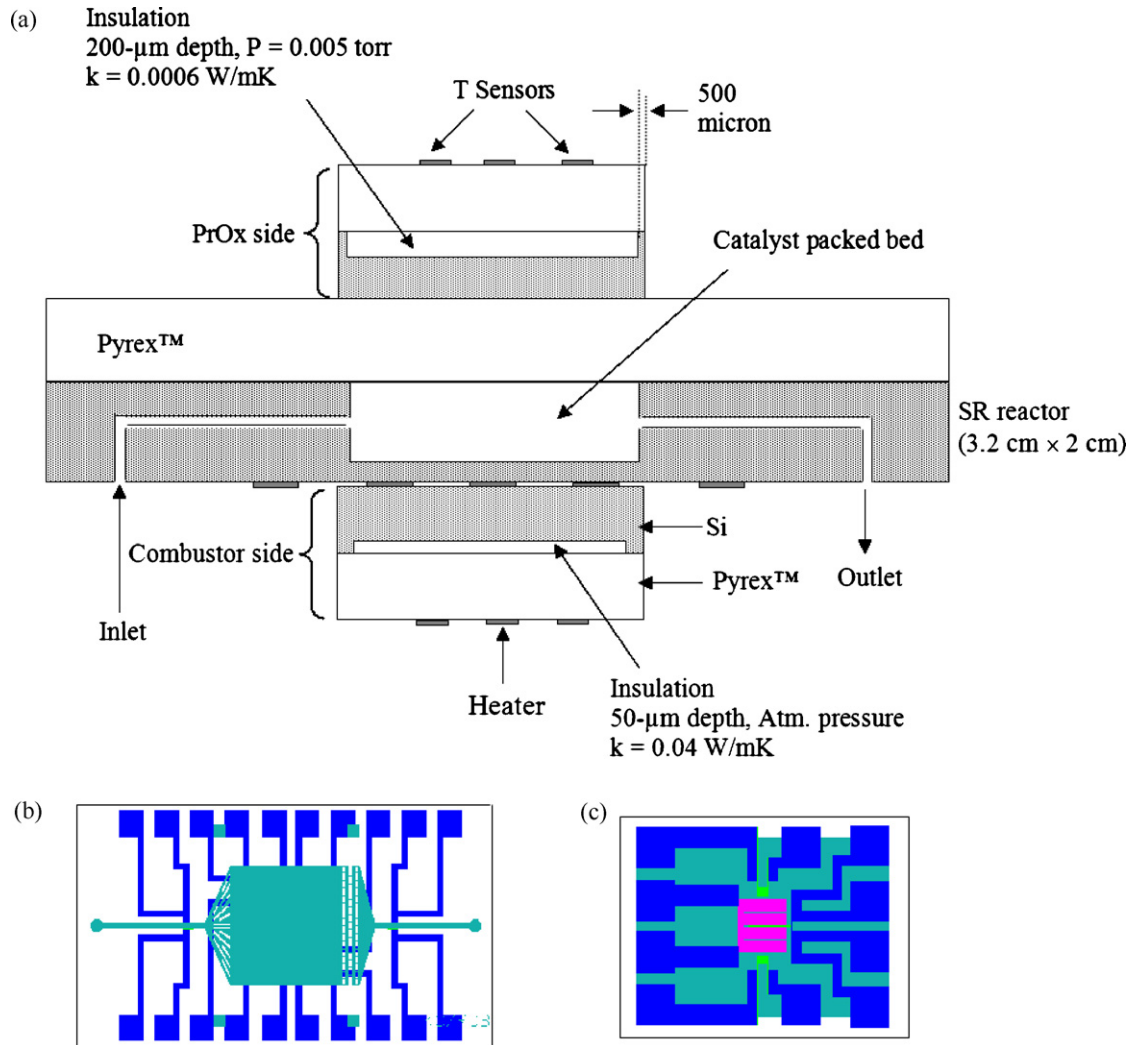
Fig. 7. (a) The design of the integrated SR. (b) Superimposed image of the front and backside CAD masks of the microreactor. (c) Mask design for silicon and glass chips of the insulation layer. Silicon chip with cavity to be etched in the center and glass chip patterned with thin film heater and temperature sensors.

($150\,\mathrm{W\,mK^{-1}}$), only a 500-μm wide border was maintained around the cavity on the silicon insulation chip to minimize vertical conduction of heat.

The effects of pressure imbalance across relatively thin slabs must be considered as this situation can result in stress accumulation and deformation of silicon or Pyrex$^{\mathrm{TM}}$. In extreme cases, fracture can result during wafer dicing to separate individual devices or later during device operation. Structural simulation was carried out with ANSYS$^{®}$ to determine the deformation and the stress formation in silicon and glass for the required vacuum inside the cavity. This simulation indicated that an 800-μm thick wafer with 200-μm cavity depth would suffice for PrOx insulation. For the designed insulation cavity chip size of $1.1\,\mathrm{cm} \times 1.4\,\mathrm{cm}$, the pressure force resulted in a predicted deformation of less than a micron in silicon and glass.

Four microreactors were fabricated on a single silicon wafer (p-type <1 0 0> 4-in. diameter, 550-μm thick, double-side polished) by silicon bulk micromachining techniques. Photolithography was employed first to pattern the front side of the microreactors using thick photoresist. These structures were then etched to a depth of $400\,\mu$m using deep reactive ion etching (DRIE) by inductively coupled plasma (ICP) [40]. A 2-μm thick silicon dioxide hard mask was used for deep silicon etching. Once the front side was processed, a second mask was used for backside patterning of inlet and outlet vias. These vias were then opened from the backside by wafer through etching with DRIE. Thin-film Pt temperature sensors were then patterned on the backside of wafer. A 10 nm Ti adhesion layer was deposited followed by 200 nm of Pt without breaking the vacuum of e-beam evaporation. The photoresist was dissolved, removing the excess Ti/Pt by lift-off, leaving the temperature sensors. The fabricated silicon wafer was then sealed with Pyrex$^{\mathrm{TM}}$ glass by anodic bonding. The bonded reactor wafers were then diced into individual microreactors.

The vacuum insulation was formed by creating first a square cavity pattern on the silicon wafer and etching to a required depth using DRIE. Thin-film heater and temperature sensors were fabricated on the Pyrex$^{\mathrm{TM}}$ glass wafers using the lift-off technique. Here, the metal lines consist of a layer of Ti (10 nm) and Pt (300 nm). The patterned glass wafer was then annealed at 650 °C
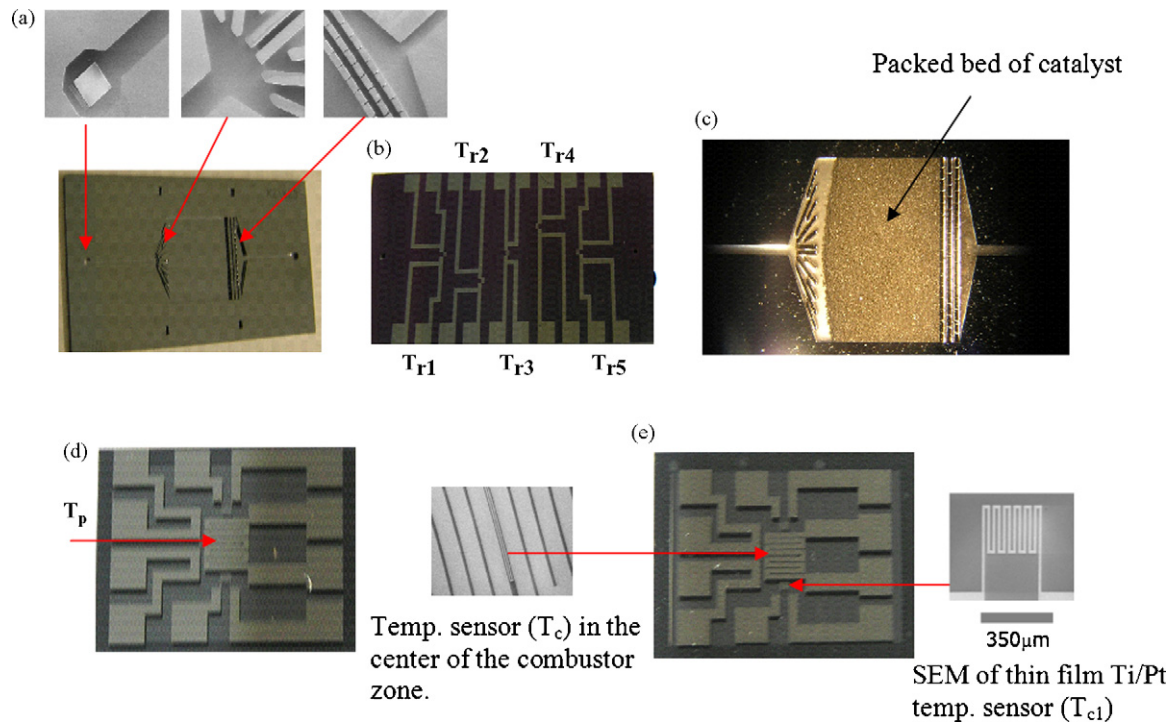
Fig. 8. (a) Frontside of silicon SR microreactor with SEM images of inlet via, flow manifold, and catalyst traps. (b) Backside of SR microreactor showing patterned temperature sensors. (c) Incorporation of catalyst in the form of packed bed by vacuum loading. Catalyst loading achieved was 53.1 mg. (d) PrOx side insulation chips. Etched cavity in silicon bonded under vacuum with patterned glass. (e) Combustor side insulation chips with SEM images of central combustor (heater) zone and temperature sensors.

for 2 h to stabilize the film resistivity. The cavity-patterned silicon wafer was then anodically bonded with the patterned glass wafer, entrapping air at the required pressure. The bonded insulation wafers were then diced into individual chips of the required sizes. Fig. 8 shows the fabricated components of an integrated SR.

3.4. Incorporation of commercial catalyst and assembly of an integrated SR

The commercial BASF catalyst is incorporated in the form of a packed bed in the silicon microreactor bonded with glass. The catalyst was received in a pellet form, and was ball milled and sieved to obtain catalyst particles of mean diameter 70–80 μm. These particles were then introduced into the reaction zone through the inlet via while creating suction at the outlet. The reactor has an array of catalyst filter structures at the outlet with a gap spacing of 30 μm ensuring that catalyst particles larger than this remain trapped within the reaction zone. Fig. 8(c) shows the silicon microreactor packed with catalyst.

Next, the insulation chips are bonded on the front and back sides of the catalyst-loaded microreactor using high temperature epoxy. Fig. 9 shows the microreactor bonded with the insulation chips.
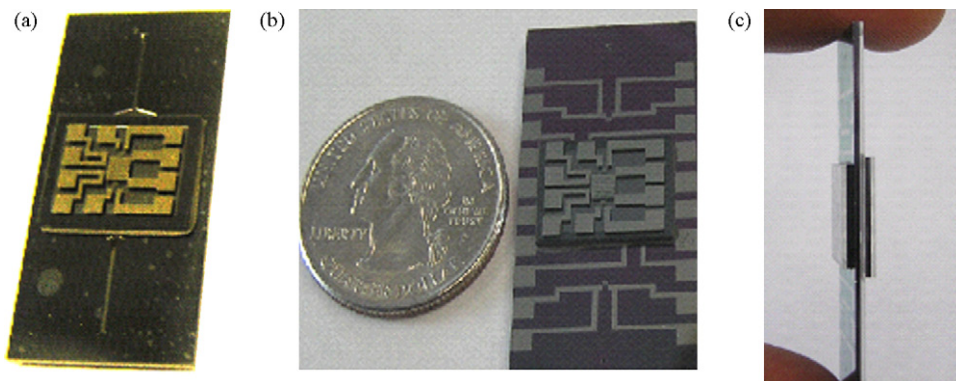

Fig. 9. SR microreactor bonded with the insulation chips. (a) Frontside of SR microreactor bonded with insulation chips. (b) Backside of reactor bonded with insulation chips. (c) Assembled integrated microreformer (six-chip stack).

4. Results and discussion

4.1. Thermal characterization

Thermal characterization of an integrated reformer was carried out without flows and reaction in order to measure critical thermal parameters including heat requirement, heat transfer rates between components, lateral and vertical temperature distributions, insulation effectiveness, and heat loss mechanisms.

Electrical connections were made by attaching thin wires to the contact pads with conductive silver epoxy. All thin-film temperature sensors were first calibrated from room temperature to 300 °C to relate the change in resistance with temperature. A linear trend was observed by plotting normalized resistance (R/R_0) versus the temperature. The temperature coefficient of resistance (TCR) was then calculated using a linear fit, which allowed estimating temperatures from the experimental resistance data.

For thermal characterization, the integrated device was not supported by any fixture to avoid external thermal contact. Instead, the device was suspended in air only by the attached wires as shown in Fig. 10.

For characterization, electrical heating with the integrated thin-film heater was carried out to introduce a well-defined rate of heating. Heating was carried out until the required 260 °C temperature was obtained in the SR reaction zone. Once the device reached steady state, the current and voltage across the heater were measured along with resistances of temperature sensors using digital multimeters. The power required to maintain the temperatures of the reaction zone and each component was thus obtained. We were able to safely introduce close to 6.8 W using this heater. At this power, however, it was only possible to obtain a temperature of 230 °C in the reforming reaction zone because of the high losses. Furthermore, we observed that increasing the power above ≈6.8 W resulted in a short circuit of the heater resistor and cracks in the glass from the combined effect of high current density and high temperature of ≈550 °C achieved within the small heater zone. Fig. 11 shows the tem-
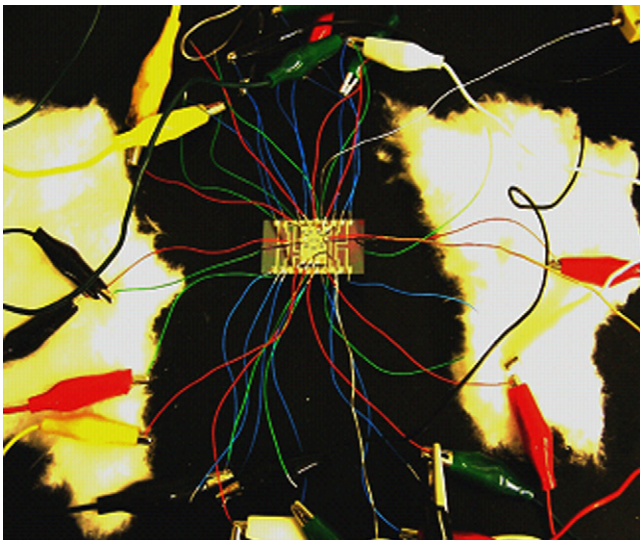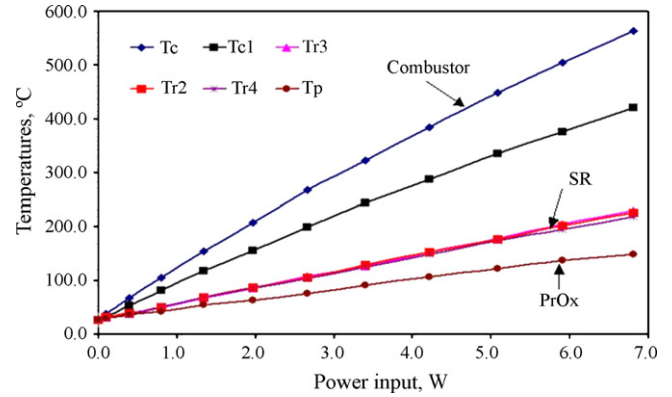

Fig. 11. Temperature obtained in different components vs. the power input to the uninsulated integrated device suspended in the ambient.

peratures of different components of the integrated device as a function of the power input to the heater.

Despite sub-optimal SR temperature reached under these condition, it was possible to obtain the required thermal isolation between the combustor, the reformer and the PrOx units. For the reformer temperature of 230 °C, the temperature obtained in the combustor and the PrOx were 564 and 150 °C, respectively. The integrated device was designed to attain 350 and 155 °C, in the combustor and PrOx respectively for the reformer temperature of 260 °C. The reaction zone remained at uniform temperature as measured by three temperature sensors ((T_{r_2}, T_{r_3}, T_{r_4}) placed at different location on the backside. This uniformity of temperature results from the high thermal conductivity of the silicon reactor embedded between insulation chips.

However, for the free surfaces open to the ambient, large lateral thermal gradients were observed even from these small-scale devices. For example, we observed a temperature difference of greater than 100 °C between a combustor (T_c, measured by a thin-film sensor placed in the center of the combustor) and T_{c1}, thin-film temperature sensor that was placed at a lateral distance of 600 μm from the combustor. Therefore, it was necessary to measure the surface temperature distributions at even higher resolution than originally planned. In addition to thin-film temperature sensors, manually placed thermocouples were used to obtain temperatures at locations intermediate to the micro RTD sensors.

Various heat loss pathways were identified and the individual contribution of these pathways was determined from the measured heat input as a function of surface temperature. Heat is lost from the free surfaces by free convection and radiation. In addition to this, heat loss through attached suspending wires and thermocouples was considered. Therefore, at steady state,

$$Q_{in} = VI = Q_{loss} = Q_{wires} + Q_{conv.} + Q_{rad.} \qquad (4)$$

Heat loss from these wires on each surface was estimated by applying the so-called pin fin theory [41]. Heat dissipated from the wires was calculated by integrating the loss over the side surface of the wires, yielding

$$Q_{wires} = \frac{(hP'(T_s - T_\infty)\tanh\alpha l)n}{\alpha} \qquad (5)$$

Fig. 10. Thermal characterization of an integrated device suspended in air.

where $\alpha = hP'/kA_w$, $P' = 2\pi R$, is the perimeter of the wire, R is the radius of the wire (250 μm), A_w the cross-sectional area of the wire, h the heat transfer coefficient = 50 W m^{-2} K^{-1} (assumed), T_s the edge temperature of the respective surface, T_∞ the ambient temperature, $l = 10$ cm, the length of wire, and n is the number of wires on each free surface.

Since the substrate media incorporated here are transparent to significant portions of the emission spectrum involved, the spectral volumetric emission and absorption in silicon and glass were taken into account. For an isothermal, absorbing and emitting medium, the intensity $I_\lambda(L)$ of a monochromatic beam of radiation is given by the following equation [42].

$$I_\lambda(L) = I_\lambda(\mathrm{o}) \, e^{-k_\lambda L} + I_{b\lambda}(1 - e^{-k_\lambda L}) \tag{6}$$

The first term, $I_\lambda(\mathrm{o}) \, e^{-k_\lambda L}$, relates to the intensity of an impinging beam and its reduction within the solid medium of thickness L due to absorption. The second term, $I_{b\lambda}(1 - e^{-k_\lambda L})$, is the volume-generated emission taking place over the thickness of material, L. For a composite of adjacent silicon and glass pieces of thickness L and L', respectively, equation (6) then can be used to determine intensity at the free surfaces of the composite. Equation (7),

$$I_\lambda(L') = I_{b\lambda}(1 - e^{-(\overset{Si}{k} L/2 + \overset{Py}{k} L')}) \tag{7}$$

gives the intensity at the free surface of the Pyrex^{TM} piece in a composite of silicon and Pyrex^{TM}. This equation can also be rewritten to obtain the intensity $I_\lambda(L)$ from the free surface of the silicon piece. In these equations, $I_{b\lambda} = E_{b\lambda}/\pi$, where $E_{b\lambda}$ is the spectral blackbody emissive power (W m^{-2} μm^{-1}) [37]. $\overset{Si}{k}$ and $\overset{Py}{k}$ are the spectral absorption coefficients of silicon and Pyrex^{TM}, respectively. These calculations are made for the wavelength range from 0.1 to 100 μm to obtain the total emissive power E (W m^{-2}), which is then multiplied by area to obtain Q_{rad}. After determination of the radiation rate, the estimated values of Q_{wires} and Q_{rad} were then subtracted from the measured heat loss to evaluate $Q_{conv.}$ as in equation (8).

$$Q_{conv} = Q_{loss} - Q_{wires} - Q_{rad} \tag{8}$$

Fig. 12 shows the steady-state heat loss due to conduction through wires, natural convection, and radiation (surface radiation and volumetric emission) as a function of SR reaction zone temperature. The heat loss estimate shows that the surface loss by what we initially considered to be typical natural convection makes up the major fraction of overall loss at atmospheric pressure.

An unexpected finding from these results is that the effective convective losses were found to be significantly higher at this length scale than the predictions obtained by correlations for objects of conventional scale. We found that the heat transfer coefficient for natural convection increases dramatically as the surface dimensions decrease and was severely under predicted in our initial estimates. Based on additional experiments and analysis, we developed the following dimensionless correlation to predict the effective heat transfer coefficient of natural convection for micro to mesoscale objects (sub-mm to mm scale).
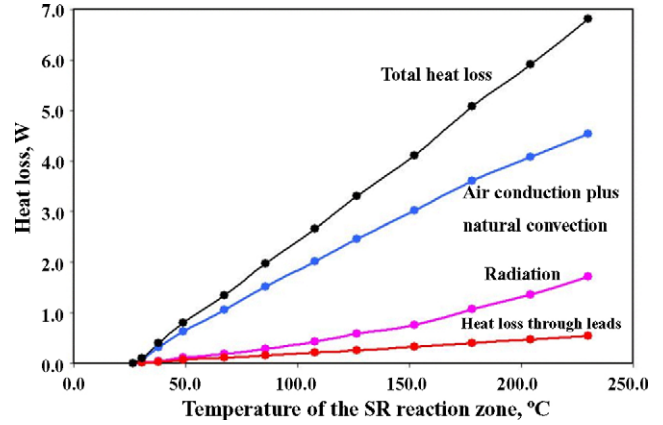

Fig. 12. Total steady-state heat loss measured experimentally and estimated heat loss by various pathways vs. the SR reaction zone temperatures.

The detailed data analysis and derivation of this correlation can be found elsewhere.

$$N_{Nu} = 1.7 N_{Ra}^{0.08} \tag{9}$$

where N_{Nu} is Nusselt number and N_{Ra} Rayleigh number. The uncertainty in predicting Nusselt numbers from these correlations is approximately ±15% attributed mainly to experimental error and assumptions made during estimation of the different losses.

The observed high convective losses to the ambient are believed to be the combined effect of air conduction and convective transport with the former dominating at this scale. When we compared the pure convective heat rate using a conventional, macroscale correlation from the literature [37], we found that it could only account for 30% of the effective transport rate. This is in agreement with the results of others who found extraordinarily high effective rates of convection from mm- to cm-scale surfaces [43,44], leading to suggestions that direct conduction in the air is responsible for the discrepancy. We adhere to this hypothesis as well, and hence the correlation we developed (equation (9)) conveys an effective convection coefficient, since we believe another process besides convection must be contributing. Gas-phase (air) conduction could be explained as significant with decreasing system size in the following way: the small volume of gas heated by a small (mm- to cm-scale) interfacial area is changed in density due to an increase in temperature. While with macroscale objects, this density difference drives the flows associated with natural convection, the buoyancy forces on the small volumes of heated gas in this case are too small to strongly overcome the forces of viscous drag which oppose the convective motion. As a result, the gas does not flow significantly, and direct conduction from the surface becomes dominant.

Thermal radiation is also important in the consideration of our measurements as it amounts to a significant fraction of loss especially at high temperatures. However, from experimental measurements of steady-state heat loss and derived correlations, we observe that gas conduction and convection dominate loss by radiation even at fairly high temperatures for small-scale devices compared to macroscale devices. For all temperature ranges measured, heat loss via the attached wires was less than 7%.
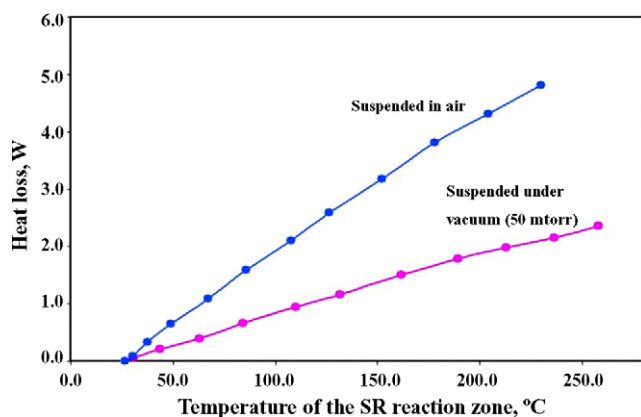
Fig. 13. Heat loss by air conduction and natural convection as a function of the SR reaction zone temperature for the integrated device suspended in air and under vacuum.

Thermal characterization of this assembled device was then carried out under vacuum to determine the effect of sub-atmospheric pressure on steady state heat loss. The integrated device resting on the attached wires was placed in the vaccum chamber. The chamber was evacuated down to 50 mTorr, and the steady-state heat losses were characterized as a function of surface temperatures.

Measurements under vacuum showed that $\approx$4.3 W was needed to obtain the required 260 °C temperatures in the SR reaction zone. The steady state heat loss data was then analyzed to determine relative magnitudes of conduction through wires, air conduction plus natural convection, and radiation losses. Fig. 13 shows the comparison of heat losses by air conduction plus natural convection as a function of SR reaction zone temperature for the ambient pressure and vacuum tests. For the SR reaction zone temperature of 230 °C, the heat loss by air conduction plus natural convection was 2.1 W under vacuum compared to 4.8 W observed at ambient pressure. Therefore, it was possible to reduce this loss by about 60%.

Additional thermal characterization experiments were carried out both at atmospheric pressure and under vacuum where the integrated device was covered in commercial fiberglass insulation. Table 3 shows the heat input and temperatures attained in combustor, SR, and PrOx zones, and a breakdown of steady-state heat losses into convective and radiative losses for each experiment.

As shown in Table 3, the device when covered in loosely packed fiberglass insulation showed the best performance at both atmospheric and vacuum tests. Losses decrease with an increase in thickness of the insulation, resulting from reduced temperature gradients and heat transfer coefficient. However, using a large quantity of insulation adds to the weight and especially volume of the overall system, which translate into reduced energy density.

4.2. Reaction characterization

Experiments are carried out to determine conversion and selectivity, hydrogen production rate (corresponding power output), heat required to drive the reforming reaction, and thermal effects on reaction.

The integrated microreformer was characterized on a custom-built test setup. A high performance liquid chromatography (HPLC) pump was used to introduce the premixed liquid reactants of water and methanol to the vaporizer. The vaporizer was built by wrapping flexible heaters around the stainless steel tube of 1/16 in outside diameter. The vaporized mixture was then fed to an inlet of the silicon microreformer placed on the interface block. Separate inlet lines are provided to introduce measured flows of nitrogen and 5% hydrogen to the microreformer for the catalyst reduction. The stainless steel reactor block was designed to ensure minimum thermal contact with the device. The product was sent to the condenser to remove unconverted water and methanol. A downstream mass flow meter was used to measure the flow rate of the dried reformate stream before it was analyzed by micro gas chromatography (Varian CP-4900). The whole tubing system was wrapped with tape heaters and insulated to prevent condensation.

Electrical connections to the exposed contact pads on the integrated thin-film heater and temperature sensors were made from outside using standard alligator clips. The vaporizer heaters, mass flow controllers, and the GC were automatically monitored and controlled by synchronizing the setup with a computer using LabView software.

Prior to the reaction, the catalyst was reduced with 2 sccm of 5% H_2/N_2 at 280 °C for 2 h. The reforming reaction was then carried out by introducing a methanol-water mixture with a 1:1.3 molar ratio at a defined rate along with a stream of 5 sccm of N_2 as an inert chromatography reference. The flow rates of H_2,

Table 3
Power required to maintain reformer temperature at 260 °C, corresponding to temperatures obtained in the combustor, SR, and PrOx zones, and breakdown of steady-state heat loss into convective and radiative losses for each experiment

Experiment	Q_{in} (W)	T_{comb} (°C)	T_{SR} (°C)	T_{PrOx} (°C)	$Q_{conv.}$ (W)	Q_{rad} (W)
Suspended on wires in ambient	6.8	564	230	149	4.8	1.7
Suspended on wires under vacuum	4.3	452	260	176	2.4	1.7
Covered with fiberglass insulation of size, $l = 4$ cm, $w = 2.3$ cm, $t = 2.4$ cm, in ambient	5.1	532	260	166	3.6	1.3
Covered with fiberglass insulation of size, $l = 4$ cm, $w = 2.3$ cm, $t = 2.4$ cm, under vacuum	2.8	414	260	186	1.3	1.3
Placed in insulation of size, $l = 10$ cm, $w = 8$ cm, $t = 8$ cm, in ambient	2.5	411	260	181	1.3	1.0
Placed in 10 cm $\times$ 8 cm $\times$ 8 cm insulation, under vacuum	1.8	386	260	181	0.6	1.0

The convective loss shown here actually accounts for the combined effect of air conduction and natural convection losses.
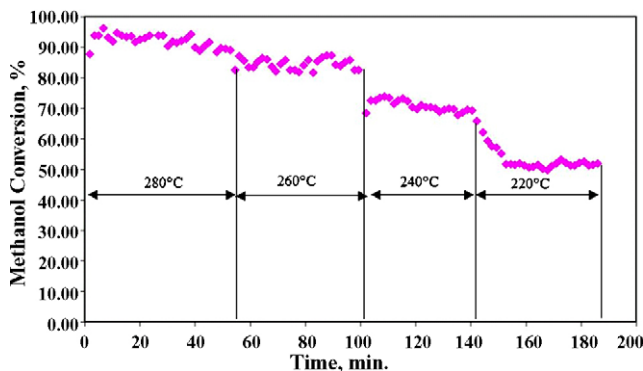
Fig. 14. Methanol conversion obtained at different temperatures. Methanol–water feed: 0.009 ml min^{-1}, S:C = 1.3:1, WHSV: 5.1 h^{-1}, GHSV: 11670 h^{-1}.

Fig. 15. Flow rates of H$_2$, CO$_2$, and CO produced as a function of methanol–water feed rate.

CO_2, and CO were obtained by relating their GC intensities to the signal from the 5 sccm N_2 flow.

Because of the relatively large thermal mass of the block and high losses, it was not possible to heat the device to the required temperature with the device's integrated thin film heater alone. Hence a tape heater was used to maintain the test block at a temperature of 150–200 °C. The integrated microreformer was then heated to a desired temperature in the SR reaction zone using the thin-film heater. The reaction was carried out at different temperatures from 220 to 280 °C with a combined feed flow rate of 0.009 ml min^{-1} (methanol flow rate of 1.36e−4 mol min^{-1}). Fig. 14 shows the methanol conversion obtained at different temperatures. At 280 °C, close to 100% methanol conversion was achieved, producing 9 sccm of H$_2$. At the reaction temperature of 220 °C, the methanol conversion decreased to 50%, reducing the H$_2$ produced to 5.2 sccm. CO was not formed in detectable amounts at the reaction temperature of 220 °C, however, it increased to 1.1% as the temperature increased to 280 °C. This CO can be further minimized to less than 10 ppm by employing PrOx microreactor to prevent poisoning of fuel cell electrodes.

We did not observe any major change in temperature profiles during the reaction arising from either the flows or the endothermic nature of the reaction. This occurred because the heat required to carry out the endothermic SR reaction is quite small relative to the amount of heat to be input (because of high heat losses) in order to maintain the required reaction temperature.

The effect of feed flow rate (and equivalently space velocity) on the methanol conversion was determined by changing combined feed flows from 0.007 to 0.015 ml min^{-1} at a reaction temperature of 260 °C. Methanol conversion was decreased, while the reformate and hydrogen flow rates increased with increasing feed flow rate (resulting in decreasing residence time). With the total feed rate of 0.015 ml min^{-1}, 82% of methanol conversion was achieved, producing 14.3 sccm of hydrogen. Considering 60% FC efficiency and 75% H$_2$ utilization, this stream is sufficient to produce 1.04 W from the FC. Fig. 15 shows the flow rates of H$_2$, CO$_2$, and CO in the reformate stream as a function of feed flow rates. Also shown are the corresponding anticipated powers from the FC. After the separation of condensibles, the concentrations of H$_2$ in the reformate
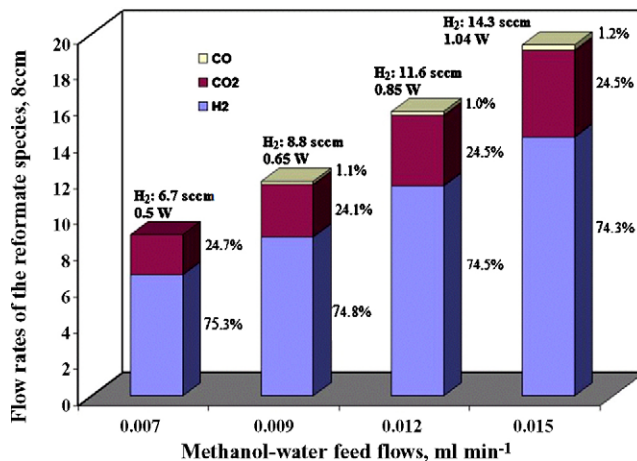
stream remained constant at 74% at all the conditions of temperature and feed flow rate. The catalyst remained stable over a reaction period of 6 h studied here, however, reaction should be carried out over greater lengths of time to evaluate catalyst performance and degradation issues.

Microreactors are known to have faster heat and mass transfer rates than conventional fixed bed reactors and are normally assumed to operate in the reaction-limited mode [45]. However, for the practical reactor system considered, it is necessary to check the influence of mass transfer on the reaction performance. We assumed the absence of internal mass transfer as it can be safely neglected for catalyst particles with a diameter smaller than 100 μm [36]. External mass transfer, involving mass transport of reactants from the bulk to the catalyst surface usually becomes important in microreactors. Based on the calculations of the diffusion coefficients, it was shown that methanol is most likely the limiting reactant in the SR reaction [46]. We employed Mears' criterion to examine the methanol mass transport limitation.

According to Mears, there is no mass transfer limitation if the following criterion is fulfilled [47]:

$$\frac{r_{MeOH}\, d_h}{2 k_g c_{MeOH}} < 0.15 \tag{10}$$

where r_{MeOH} is the measured reaction rate, d_h the hydraulic diameter of the reaction zone, k_g the mass transfer coefficient, and r_{MeOH} is the methanol concentration in the feed.

Due to the small hydraulic diameter and low flow rates involved, the flow in the microreactor was laminar. The mass transfer coefficient was determined by considering that in the fully developed laminar flow, the Sherwood number Sh approaches a constant value.

$$Sh = \frac{k_g d_h}{D_{AB}} = 3.66 \tag{11}$$

where D_{AB} is the diffusivity of methanol in the gas mixture, calculated on the basis of mole fractions of the species in the gas mixture [48].
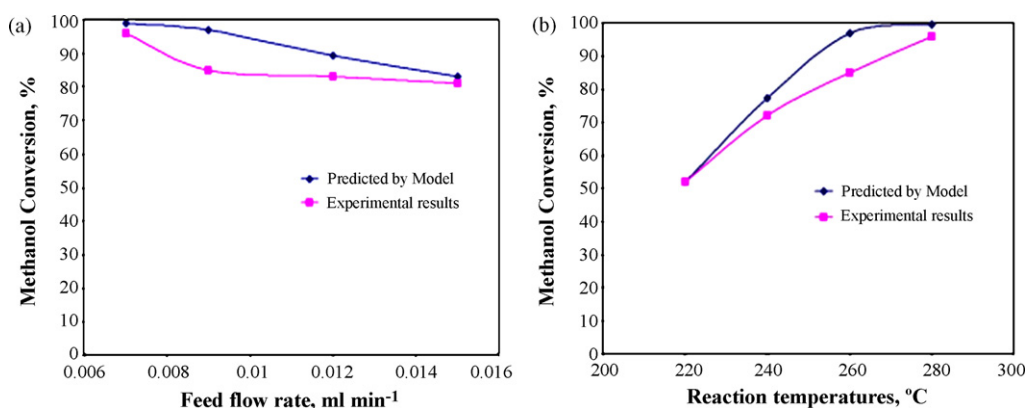
Fig. 16. Methanol conversion predicted by simulation and measured experimentally (a) as a function of feed flow rate with a reaction temperature of 260 °C, (b) as a function of temperatures with a feed rate of 0.009 ml min^{-1}.

The value of $r_{MeOH} d_h/2k_g c_{MeOH}$ estimated was 7.5e−2, which implies that there was no external mass transport limitation. Fig. 16(a) and (b) shows the comparison between the methanol conversion measured and predicted by the kinetic model at different temperatures and flow rates, respectively. The experimental conversion obtained matched reasonably with that predicted by a kinetic model based on the literature kinetic expression, neglecting mass transfer resistance. This further corroborates the absence of external mass transport limitation, confirming that the reaction was rate limiting.

4.3. Packaging suggestions and scale up

Based on the understanding gained from thermal characterization experiments, packaging suggestions are made to reduce air conduction, convection, and radiation losses.

- In scaling up, it is desirable to form a stacked three-dimensional assembly in preference to using larger layers (3D architecture instead of planar sheets). This reduces the surface-to-volume ratio and thus the surface convective and radiative losses.
- Heat losses by air conduction and natural convection constitute a significant fraction of total heat loss at ambient pressure. These heat losses were reduced by covering the device in insulation and operating under vacuum. Use of low-k insulating materials helps reduce these losses. However, there is a trade-off on the amount of insulation that can be used without adding much to the weight and volume of the integrated system. Additionally, it would be helpful to use a low-k gas like argon instead of air surrounding the integrated device to reduce gas conduction losses. We observed that the use of vacuum below 50 mTorr reduces these losses by at least 60%. However, at this level of vacuum, the air conduction and convection could not be entirely suppressed. This is consistent with other reports in literature [32,35]. Vacuum packaged insulation is superior for reducing these heat losses without significantly increasing volume. However, it seems that a vacuum down to 10^{-4} Torr or below is required to minimize losses through the ambient air [32]. This presents a challenge in developing a reliable

and hermetic vacuum package that can hold such a low pressure for a long period of time. We suggest employing both low-k insulating material and vacuum packaging to reduce air conduction and convective losses.
- Radiative heat losses from a free surface can be reduced by using reflective insulation or by employing high reflectivity and low emissivity materials.

We observed that heat loss to the ambient via gas conduction, convection, and radiation was substantial compared to the required heat for critical energy-consuming FP functions including fuel vaporization and the endothermic SR reaction. Considering the integrated device of the vaporizer, combustor, SR, and PrOx having a size of $1 \, cm \times 1 \, cm \times 0.5 \, cm$, if we employ the above packaging recommendations, it would still result in a minimum heat loss of 1.0 W. The total energy required considering heat loss (1.0 W) plus energy to drive the endothermic SR reaction (0.13 W) and fuel and water vaporization (0.20 W) is then 1.33 W. Considering 75% hydrogen utilization in the FC, hydrogen recycled from the FC anode when burned gives only 0.38 W, thus an additional 1.33−0.38 = 0.95 W would required by combusting methanol fuel. The device can produce 3.84e−4 mol min^{-1} of hydrogen, resulting in a lower
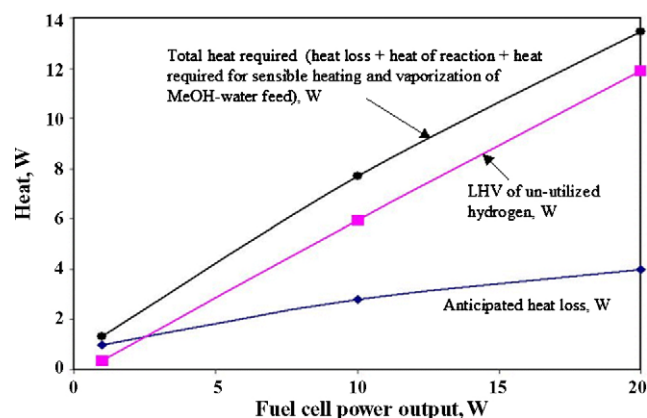

Fig. 17. Anticipated heat loss, reformer energy requirement, and LHV of the un-utilized hydrogen in the anode-off gas as a function of FC power output.

heating value (LHV) of 1.55 W, while considering FC efficiency as mentioned previously it can produce a net 0.65 W output. Thus we will begin to see the benefits of an integrated FP/FC approach as systems are designed for powers exceeding a few W. Fig. 17 shows the anticipated heat loss after stacking of reactor layers and employing packaging recommendations, including the heat duty required for endothermic SR reaction and for fuel and water vaporization, and the LHV of un-utilized hydrogen available at different power outputs of 1, 10, and 20 W from the FC.

5. Conclusions

Understanding thermal management issues in a portable FP is crucial in order to reduce heat losses and improve thermal efficiency. We implemented silicon microchemical systems to investigate thermal integration of FP reactor components with a methanol SR as a model. The fabricated model components of an integrated microchemical device were used for the acquisition of critical thermal parameters of the overall coefficients for the transfer of heat from components to one another and to the outside environment by various heat loss pathways. Based on thermal characterization experiments, the heat loss mechanisms and the effective convective heat coefficient were determined and suggestions were made for scale up and implementation of packaging schemes to reduce different modes of heat loss. Acquisition of the thermal experimental data helped to verify and improve the model used to simulate the system. This combined experimental/modeling approach can then be used as the quantitative basis for designing an integrated portable FP.

The SR microreactor produced 14.3 sccm of hydrogen (corresponding to a net power output of 1.04 W from the FC) with relatively low levels of carbon monoxide. The results effectively demonstrate the potential of microreactor-based on-demand H_2 generation, and provide impetus for a subsequent phase of development involving completely integrated subsystems.

Acknowledgements

References

[1] Fuel Cell Handbook, fifth ed., Report prepared by EG&G Services for the US Department of Energy, National Energy Laboratory, October 2000.
[2] C.K. Dyer, J. Power Sources 106 (1–2) (2002) 31–34.
[3] A.S. Patil, T.G. Dubois, N. Sifer, E. Bostic, K. Gardner, M. Quah, C. Bolton, J. Power Sources 136 (2004) 220–225.
[4] K. Kordesch, G. Simader, Fuel Cells and Their Applications, VCH, Germany, 1996.
[5] D.G. Loffler, K. Tylor, D. Mason, J. Power Sources 117 (1–2) (2003) 84–91.
[6] B. Lindstrom, L.J. Pettersson, J. Power Sources 118 (2003) 71–78.
[7] Q. Ming, T. Healey, L. Allen, P. Irving, Catal. Today 77 (2002) 51–64.
[8] A. Ming, J. Wu, Q. Wang, Int. J. Hydrogen Energy 20 (2) (1995) 141–150.
[9] R. Dillon, S. Srinivasan, A.S. Arico, V. Antonucci, J. Power Sources 127 (1–2) (2004) 112–126.
[10] S. Song, P. Tsiakaras, Appl. Catal. B: Environ. 63 (3–4) (2006) 187–193.
[11] S. Aravamudhan, A.R. Abdur, S. Bhansali, Sens. Actuators A: Phys. 123–124 (2005) 497–504.
[12] S. Ha, B. Adams, R.I. Masel, J. Power Sources 128 (2) (2004) 119–124.
[13] S. Ha, Z. Dunbar, R.I. Masel, J. Power Sources 158 (1) (2006) 129–136.
[14] C. Song, Catal. Today 77 (1–2) (2002) 17–49.
[15] P.J. de Wild, M.J.F.M. Verhaak, Catal. Today 60 (1) (2000) 3–10.
[16] B.A. Peppley, J.C. Amphlett, L.M. Kearns, R.F. Mann, Appl. Catal. A 179 (1–2) (1999) 21–29.
[17] K. Shah, R.S. Besser, Chem. Eng. Technol. 28 (3) (2005) 303–313.
[18] R. Nowak, DoD end user perspective & DARPA palm power program, Presented at the DOE Fuel Cell Portable Power Workshop, Phoenix, AZ, USA, 2002.
[19] W. Ehrfeld, V. Hessel, H. Lowe, Microreactors: New Technology for Modern Chemistry, Wiley-VCH, Weinheim, 2000.
[20] R.S. Besser, X. Oyuang, H. Surangalikar, Chem. Eng. Sci. 58 (2003) 19–26.
[21] D.Y. Qian, R.S. Besser, A. Lawal, Proceedings of the AIChE Spring National Meeting, Orlando, FL, 2006.
[22] H. Chen, L. Bednarova, R.S. Besser, W.Y. Lee, Appl. Catal. A: Gen. 286 (2) (2005) 186–195.
[23] S.R. Samms, R.F. Savinell, J. Power Sources 112 (2002) 13–29.
[24] R.W. Schefer, Combust. Flame 45 (1982) 171–190.
[25] X. Ouyang, L. Bednarova, R.S. Besser, P. Ho, AIChE J. 51 (6) (2005) 1758–1772.
[26] H. Chen, W.Y. Lee, J. Am. Ceram. Soc. 90 (1) (2007) 36–43.
[27] D.J. Seo, W.L. Yoon, Y.G. Yoon, S.H. Park, G.G. Park, C.S. Kim, Electrochim. Acta 50 (2–3) (2004) 719–723.
[28] J.D. Holladay, J.S. Wainright, E.O. Jones, S.R. Gano, J. Power Sources 130 (2004) 111–118.
[29] E.R. Delsman, M.H.J.M. de Croon, G.J. Kramer, P.D. Cobden, Ch. Hofmann, V. Cominos, J.C. Schouten, Chem. Eng. J. 101 (1–3) (2004) 123–131.
[30] A.V. Pattekar, M.V. Kothare, J. Microelectromech. Syst. 13 (1) (2004) 7–18.
[31] Y. Kawamura, N. Ogura, T. Yamamoto, A. Igarashi, Chem. Eng. Sci. 61 (2006) 1092–1101.
[32] L.R. Arana, S.B. Schaevitz, A.J. Franz, M.A. Schmidt, K.F. Jensen, J. Microelectromech. Syst. 12 (5) (2003) 600–612.
[33] S. Tanaka, J.S. Chang, K. Min, D. Satoh, K. Yoshida, M. Esashi, Chem. Eng. J. 101 (1–3) (2004) 143–149.
[34] J.A. Hallmark, Presented at The Knowledge Science Foundation's 5th International Small Fuel Cells 2003: Small Fuel Cells for Portable Power Applications, New Orleans, LA, 2003.
[35] T. Terazaki, M. Nomura, K. Takeyama, O. Nakamura, T. Yamamoto, J. Power Sources 145 (2005) 691–696.
[36] H. Scott Fogler, Elements of Chemical Reaction Engineering, third ed., Prentice-Hall, NJ, 2000.
[37] F.P. Incropera, D.P. Dewitt, Fundamental of Heat and Mass Transfer, fifth ed., John Wiley & Sons, NY, 2001.
[38] P. Atkins, J.D. Paula, Physical Chemistry, seventh ed., W.H. Freeman & Company, NY, 1997.
[39] Clemens J.M. Laasance, Electronics Cooling Magazine, 8 (4) (2002), http://www.electronics-cooling.com/html/2002_november_techdata.html.
[40] R.S. Besser, W.C. Shin, J. Vac. Sci. Technol. B 21 (2) (2003) 912–915.
[41] A.F. Mills, Basic Heat and Mass Transfer, Prentice Hall, NJ, 1999, pp. 293–314.

[42] A. Bejan, A.D. Kraus, Heat Transfer Handbook, John Wiley & Sons, NY, 2003.

[43] A. Giani, F. Mailly, R. Bonnot, F. Pascal-Delannoy, A. Foucaran, A. Boyer, Microelectron. J. 33 (2002) 619–625.

[44] X. Hu, A. Jain, K.E. Goodson, Proceedings of the ASME Summer Heat Transfer Conference, San Francisco, CA, USA, 2005, pp. 641–644.

[45] St. Walter, St. Malmberg, B. Schmidt, M.A. Liauw, Catal. Today 110 (2005) 15–25.

[46] A. Kolbl, P. Pfeifer, M. Kraut, K. Schubert, M. Fichtner, M.A. Liauw, G. Emig, Chem. Eng. Technol. 27 (6) (2004) 671–675.

[47] D.E. Mears, Ind. Eng. Chem. Process Des. Dev. 10 (1971) 541–547.

[48] R.H. Perry, D. Green, Perry's Chemical Engineers' Handbook, sixth ed., McGraw-Hill, New York, 1984.